

The 300-pc Scale ALMA View of [C I] $^3P_1-^3P_0$, CO $J = 1-0$, and 609 μm Dust Continuum in A Luminous Infrared Galaxy

T. Saito,^{1*} T. Michiyama,² D. Liu,¹ Y. Ao,^{3,4} D. Iono,^{2,5} K. Nakanishi,^{2,5}
E. Schinnerer,¹ K. Tadaki,² J. Ueda,² and T. Yamashita²

¹Max Planck Institute for Astronomy, Königstuhl 17, 69117 Heidelberg, Germany

²National Astronomical Observatory of Japan, 2-21-1 Osawa, Mitaka, Tokyo 181-8588, Japan

³Purple Mountain Observatory, Chinese Academy of Sciences, Nanjing 210008, China

⁴School of Astronomy and Space Science, University of Science and Technology of China, Hefei, Anhui, China

⁵The Graduate University for Advanced Studies (SOKENDAI), 2-21-1 Osawa, Mitaka, Tokyo 181-0015, Japan

Accepted XXX. Received YYY; in original form ZZZ

ABSTRACT

We present high-quality ALMA Band 8 observations of the [C I] $^3P_1-^3P_0$ line and 609 μm dust continuum emission toward the nearby luminous infrared galaxy (LIRG) IRAS F18293-3413, as well as matched resolution (300-pc scale) Band 3 CO $J = 1-0$ data, which allow us to assess the use of the [C I] $^3P_1-^3P_0$ line as a total gas mass estimator. We find that the [C I] line basically traces structures detected in CO (and dust), and a mean (median) [C I]/CO luminosity ($L'_{[\text{C I}]} / L'_{\text{CO}}$) ratio of 0.17 (0.16) with a scatter of 0.04. However, a pixel-by-pixel comparison revealed that there is a radial $L'_{[\text{C I}]} / L'_{\text{CO}}$ gradient and a superlinear L'_{CO} vs. $L'_{[\text{C I}]}$ relation (slope = 1.54 ± 0.02) at this spatial scale, which can be explained by radial excitation and/or line opacity gradients. Based on the molecular gas masses converted from the dust continuum emission, we found that the CO-to- H_2 and [C I]-to- H_2 conversion factors are relatively flat across the molecular gas disk with a median value of $3.5^{+1.9}_{-1.3}$ and $20.7^{+9.2}_{-4.9} M_{\odot} (\text{K km s}^{-1} \text{pc}^2)^{-1}$, respectively. A non-LTE calculation yields that typical molecular gas properties seen in nearby (U)LIRGs ($n_{\text{H}_2} = 10^{3-4} \text{ cm}^{-3}$, $T_{\text{kin}} \sim 50 \text{ K}$, and $X_{\text{C I}} = (0.8-2.3) \times 10^{-5}$) can naturally reproduce the derived [C I]-to- H_2 conversion factor. However, we caution that a careful treatment of the physical gas properties is required in order to measure H_2 gas mass distributions in galaxies using a single [C I] line. Otherwise, a single [C I] line is not a good molecular gas estimator in a spatially resolved manner.

Key words: galaxies: individual: IRAS F18293-3413 – galaxies: ISM – submillimetre: ISM

1 INTRODUCTION

The lowest rotational transition of carbon monoxide (^{12}CO $J = 1-0$, hereafter CO (1–0) line) is the most common total H_2 gas mass tracer for extragalactic objects (Bolatto et al. 2013), as cold H_2 emission is not observable due to no permanent dipole moment. The low critical density of CO (1–0) ($\sim 10^{2.5} \text{ cm}^{-3}$ at kinetic temperature $T_{\text{kin}} = 40 \text{ K}$) and the high abundance of CO relative to H_2 ($\sim 10^{-4}$; Blake et al. 1987) make this line an ideal tracer for the bulk of molecular gas in galaxies. Its rest frequency (115.27120 GHz) in the millimeter (mm) window with high atmospheric trans-

mission promises easy access from the ground. Empirically, a conversion from CO (1–0) line luminosity to total H_2 gas mass, known as $\alpha_{\text{CO}(1-0)}$, is found to be rather constant in Galactic molecular clouds assuming virial equilibrium and using the large velocity gradient approximation (e.g. Young, & Scoville 1984), while nearby (ultra-)luminous infrared galaxies (LIRGs and ULIRGs) show ~ 5 times lower values (e.g., Downes, & Solomon 1998). These variations complicate the application of $\alpha_{\text{CO}(1-0)}$ in different types of galaxies, from local to high-redshift. Moreover, observations of the relatively low-frequency CO (1–0) line are more challenging for high-redshift galaxies compared to higher- J CO lines (Solomon, & Vanden Bout 2005; Carilli, & Walter 2013, and references therein). Thus high-redshift studies

* E-mail: saito@mpia.de

have to rely on an assumed higher- J CO to CO (1–0) luminosity ratio in order to measure total H_2 gas mass.

Therefore, several other molecular gas mass tracers have been proposed and their usability has been discussed for more than two decades. For example, the lower forbidden 3P fine structure line of atomic carbon ([C I] $^3P_1\text{--}^3P_0$, hereafter [C I] (1–0) line) has been proposed, alternative to the CO lines due to its easier accessibility in the mm window for high-redshift galaxies (e.g., Barvainis et al. 1997; Weiß et al. 2003; Papadopoulos et al. 2004; Alaghband-Zadeh et al. 2013; Bothwell et al. 2017; Tadaki et al. 2018; Hodge & da Cunha 2020; Valentino et al. 2020), and this line is the main target of this paper.

The rest frequency of [C I] (1–0) line (492.16065 GHz) allows, for example, a receiver covering 2mm and 3mm windows to detect high-redshift galaxies at $z = 2.0\text{--}4.8$ depending on the atmospheric transmission. As the critical density is similar to that of the CO (1–0) line ($\sim 10^{2.7} \text{ cm}^{-3}$ at $T_{\text{kin}} = 40 \text{ K}$), the [C I] (1–0) line could be a better tracer of total H_2 gas mass in high-redshift systems than higher- J CO lines, which may no longer trace diffuse, cold molecular gas in starburst galaxies (e.g., Rangwala et al. 2011). As reported by observational studies for Galactic molecular clouds (Phillips, & Huggins 1981; Ojha et al. 2001; Oka et al. 2001; Tanaka et al. 2011; Shimajiri et al. 2013), the [C I] (1–0) emission appears to coincide with CO (1–0) emission at $\sim 0.1\text{--}1\text{-pc}$ scale resolution. These observational results are inconsistent with the classical view of photodissociation regions (PDRs; Hollenbach, & Tielens 1997). In classical PDR theories, ultraviolet (UV) photon flux from young, hot stars is sufficient to control the physical properties of the cold interstellar medium (ISM), and thus the ISM properties strongly vary as a function of the distance from UV sources, forming $\text{C}^+/\text{C}/\text{CO}$ layers between the diffuse and dense gas phases. However, recent numerical simulations predict that the atomic carbon abundance significantly increases throughout clouds in star-forming galaxies as the cosmic ray ionization rate is expected to be much higher (i.e., cosmic rays can penetrate into and efficiently ionize the cold ISM), and thus C I coincides with CO (e.g., Offner et al. 2014; Glover, & Clark 2016; Bisbas et al. 2017; Papadopoulos et al. 2018; Clark et al. 2019).

These studies provide observational and theoretical evidence that support the application of the [C I] (1–0) line as a total H_2 gas mass tracer similar to the CO (1–0) line (see also Papadopoulos, & Greve 2004). However, only very few studies in the literature used high quality maps to test the large-scale (kpc-scale) correlation between [C I] (1–0) and CO (1–0) within galaxy disks, which can differ from the spatial correlation seen within molecular clouds, as most of the previous works focused on galaxy-to-galaxy variations using single-dish data (e.g., Jiao et al. 2017), central regions ($<1 \text{ kpc}$) of nearby galaxies (e.g., Krips et al. 2016; Izumi et al. 2018; Miyamoto et al. 2018), and unresolved or marginally-resolved nearby and high-redshift sources (e.g., Hughes et al. 2017; Jiao et al. 2019; Nesvadba et al. 2019).

In addition to the [C I] (1–0) line, the Rayleigh-Jeans part of the thermal dust continuum emission at mm and sub-mm wavelengths have started to be employed as an independent total H_2 gas mass tracer for high redshift galaxies based on an empirically calibrated relation be-

tween optically-thin cold dust emission and the mass of interstellar dust and gas in local star-forming galaxies, the Milky Way, and submillimeter galaxies (SMGs) (e.g., Eales et al. 2012; Scoville et al. 2014; Groves et al. 2015; Liu et al. 2019). This approach takes advantages of the higher sensitivity of mm/sub-mm facilities to continuum emission, allowing us to efficiently establish a large sample of high redshift star-forming galaxies (e.g. Aravena et al. 2016; Hodge & da Cunha 2020). However, the general spatially-resolved (kpc-scale) properties of CO and dust emission in extragalactic objects, especially starburst galaxies such as (U)LIRGs as a local counterpart of high redshift SMGs, are not fully understood yet (e.g., Iono et al. 2007; Wilson et al. 2008; Sakamoto et al. 2014; Saito et al. 2015).

In this paper, we present high-quality Atacama Large Millimeter/submillimeter Array (ALMA) Band 3 and 8 observations toward the disk ($\sim 4.5 \text{ kpc}$ in diameter) of a nearby LIRG at $\sim 300 \text{ pc}$ resolution. The 300 pc resolution matches to one of the largest molecular gas structures seen in merging galaxies (e.g., NGC 4038/9), giant molecular associations (a few 100 pc ; Wilson et al. 2000; Ueda et al. 2012). Our goals are to provide a direct comparison among [C I] (1–0), CO (1–0), and thermal dust continuum emission within the gas disk of a galaxy with well below kpc resolution and sufficient sensitivity and to test whether the [C I] (1–0) line can be used as a total H_2 gas mass tracer for spatially-resolved studies on extragalactic objects or not.

Our target, IRAS F18293-3413, is one of the nearby LIRGs classified as an H II galaxy ($D_L = 86.0 \text{ Mpc}$ and $L_{\text{IR}} = 10^{11.88} L_\odot$; Armus et al. 2009). It is a mid-to-late stage merger with an elliptical companion galaxy at a projected distance of $\sim 4.5 \text{ kpc}$. Several hard X-ray works suggested that there is no strong AGN contributing to the X-ray spectrum (e.g., Risaliti et al. 2000). This is consistent with the multi-wavelength study done by Herrero-Illana et al. (2017), which concluded that a possible AGN contribution to the total luminosity is less than 0.2%. The total star formation rate (SFR) derived from Paschen α emission and spectral energy distribution (SED) fitting is $\sim 100 M_\odot \text{ yr}^{-1}$ (Tateuchi et al. 2015; Shangguan et al. 2019). The SED fitting yields that the total stellar mass is $\sim 10^{10.94} M_\odot$, implying ~ 2 dex higher log (SFR) compared to the local main-sequence galaxies (Saintonge et al. 2016). The apparent brightness, thanks to the extremely high SFR, and the relatively face-on molecular gas disk, makes it a primary target to study the [C I], CO, and dust continuum emission with high signal-to-noise ratios.

This paper is organized as follows. We briefly summarize the ALMA data and the procedure of data reduction in Section 2. Section 3 provides image properties via pixel-by-pixel comparison. Then, we discuss the capability of the [C I] (1–0) line to trace total H_2 gas mass in Section 4, and briefly summarize our findings in Section 5. We have adopted $H_0 = 70 \text{ km s}^{-1} \text{ Mpc}^{-1}$, $\Omega_m = 0.3$, and $\Omega_\Lambda = 0.7$ throughout this paper.

2 ALMA OBSERVATIONS

The ALMA 12m and Atacama Compact Array 7m observations of Band 8 [C I] (1–0) toward IRAS F18293-3413 were carried out for ALMA cycle 3 and 6 programs, respectively

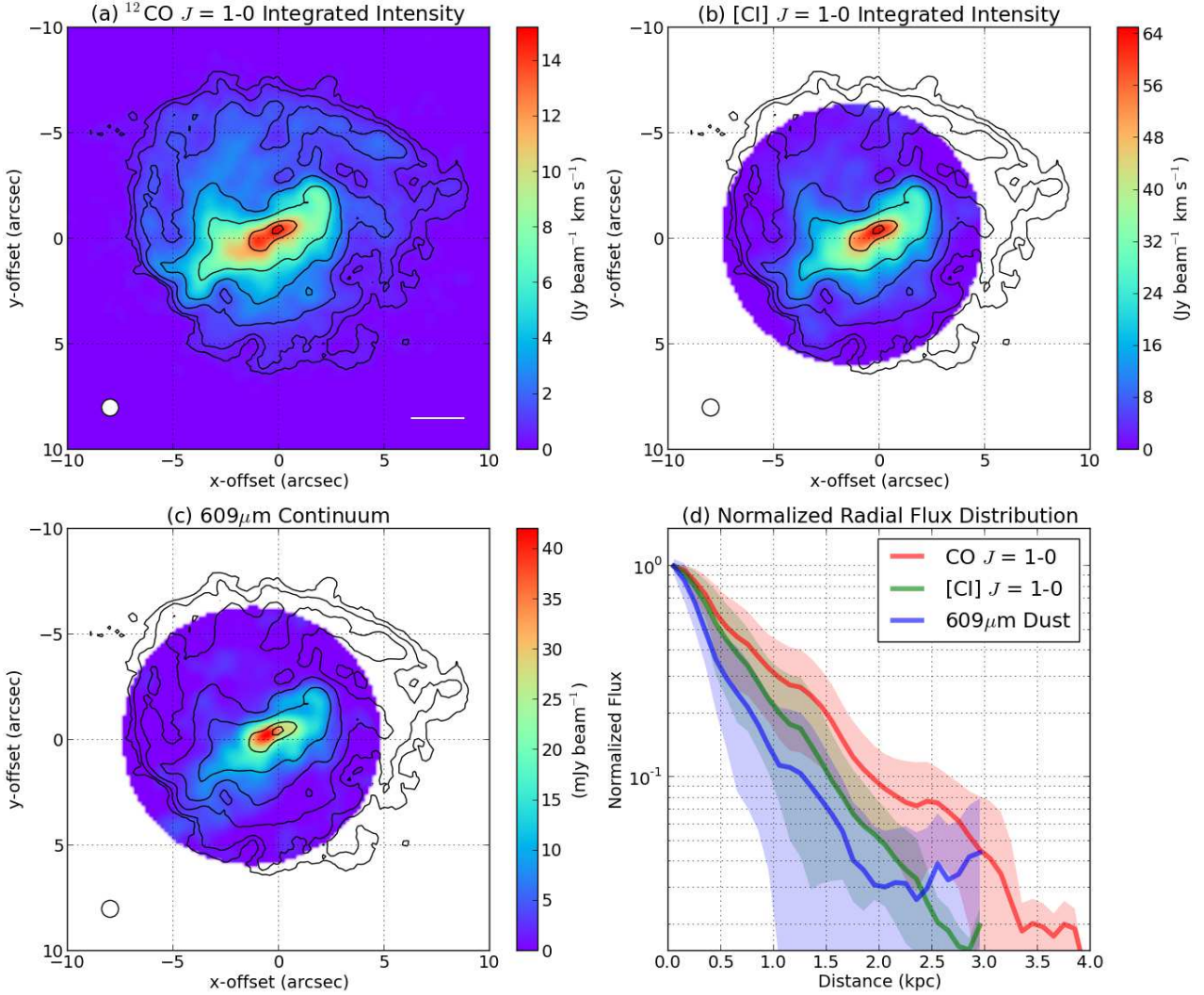


Figure 1. (a) The CO (1–0) integrated intensity image of IRAS F18293-3413. The contours are $(0.025, 0.05, 0.1, 0.2, 0.4, 0.8, \text{ and } 0.95) \times 15.2 \text{ Jy beam}^{-1} \text{ km s}^{-1}$. The convolved synthesized beam size is shown in the lower left corner. The scale bar in the lower right corner corresponds to 1 kpc. (b) The [C I] (1–0) integrated intensity image. The contours are the same as in panel (a). (c) The $609 \mu\text{m}$ continuum image. The contours are the same as in panel (a). Note that all images shown here are after correcting for primary beam attenuation. (d) Azimuthally-averaged, normalized radial flux distributions of the CO (1–0), [C I] (1–0) and $609 \mu\text{m}$ continuum images of IRAS F18293-3413. The shaded areas show the standard deviation of the distributions. The extent of the [C I] and dust profiles are limited to the Band 8 FoV (= half power beamwidth).

(ID: 2015.1.01191.S; PI = Z. Zhang, and 2018.1.00994.S; PI = T. Michiyama). These observations were tuned to the redshifted [C I] (1–0) emission line ($\nu_{\text{obs}} = 483.37293 \text{ GHz}$).

The ACA 7m Band 8 data were obtained on 2019 May 24th using eleven 7m antennas with a projected baseline length of 8.5–47.0 m and an on-source integration time of 5.03 minutes. The 7m correlator was configured to have four spectral windows (SPWs), two of which were set to each sideband, and each of the SPWs with a 2.000 GHz bandwidth and 15.625 MHz resolution ($\sim 9.7 \text{ km s}^{-1}$). The bright quasar J1924-2914 was observed as flux and bandpass calibrators. J1802-3940 and J1733-3722 were observed as phase calibrator and check source, respectively.

The ALMA 12m Band 8 data were obtained on 2016 March 28th using forty-two 12m antennas with a projected baseline length of 14–450.0 m and an on-source integration

time of 11.32 minutes. The 12m correlator was also configured to have four SPWs. Two of them were set to each sideband, and three of them have a 2.000 GHz bandwidth and 15.625 MHz resolution ($\sim 9.7 \text{ km s}^{-1}$), whereas the another one containing the [C I] line has a 1.875 GHz bandwidth with 0.488 MHz resolution. Pallas, J1924-2914, J1802-3940, and J1826-3650 were observed as flux calibrator, bandpass calibrator, phase calibrator, and check source, respectively.

The ALMA 12m Band 3 data were obtained on 2016 July 25th as a part of the Cycle 3 data described above. Forty-four 12m antennas were used to cover projected baselines of 12.3–1076.1 m length. The Band 3 receivers were tuned to cover the redshifted CO (1–0) line ($\nu_{\text{obs}} = 113.21299 \text{ GHz}$). Two of four SPWs were set to each sideband, and all SPWs have a 1.875 GHz with 0.977 MHz

(~ 2.6 km s $^{-1}$) resolution. Pallas, J1924-2914, J1826-3650 are used as a flux, bandpass, and phase calibrator.

We performed calibration and imaging (`tclean`) using the software `CASA` (version 4.5.2 and 5.4.0; McMullin et al. 2007). We ran the observatory-provided calibration pipeline with a few manual data flagging. Images were reconstructed with a natural and Briggs (robust = 0.5) weighting for the Band 8 data (i.e., C I and continuum) and Band 3 data (i.e., CO), respectively. We made datacubes with a velocity resolution of 10 km s $^{-1}$. Continuum emission was subtracted in the uv -plane by fitting the line-free channels in all available SPWs with a first order polynomial function. The line-free channels were used to create a continuum image using the multi-frequency synthesis method (`mfs`). After the imaging procedure, all datacubes and continuum image were convolved to 0''.8 resolution (~ 300 pc) for the sake of simplicity, which is slightly larger than the major axis of the clean beam of the CO (1-0) data. Then, we resampled the data onto a grid with 0''.18 pixel size, corresponding to oversampling by a factor of ≈ 4.53 ($\approx \pi/\ln 2$).

The noise rms per channel of the CO (1-0) datacube is 2.5 mJy beam $^{-1}$, which is better than that of the [C I] (1-0) datacube (5.5 mJy beam $^{-1}$). The continuum data has a noise rms of 0.75 mJy beam $^{-1}$. The systematic errors on the absolute flux calibration using a solar system object are estimated to be 5% and 20% for both sidebands in Band 3 and Band 8, respectively.

In order to create integrated intensity maps, we first convolved the CO datacube to a round 1''.0 resolution, then create a signal mask (i.e., True/False mask) with pixels larger than 3σ level. We repeated the procedure for a datacube convolved to 3''.5 resolution, and applied a 5σ level. Next, we created a combined mask using pixels where both masks are True. This masking procedure allows us to pick strong detections with surrounding weak emission which are hard to see in the original datacubes, and at the same time, we avoid inclusion of faint isolated patchy structures which are typical spurious structures. Finally, we collapsed the original 0''.8 resolution datacubes by applying the combined mask and 2σ threshold. The products are shown in Figure 1.

3 RESULTS

3.1 Spatial Distributions

In Figure 1a-c, we show the 0''.8 (~ 300 pc) resolution moment-0 maps of the CO (1-0) and [C I] (1-0) lines plus the 609 μ m continuum map. The [C I] (1-0) line and a continuum emission basically trace well structures present in CO (1-0) line emission, simply implying that the [C I] line as well as the cold dust continuum can be used as a tracer of extragalactic molecular gas mass.

The total integrated flux of [C I] (1-0) is 1550 ± 310 Jy km s $^{-1}$. The total integrated flux of CO (1-0) inside the field of view (FoV) of the Band 8 data ($\sim 13''$ 0 in full width at half maximum) is 472 ± 24 Jy km s $^{-1}$, which is 87% of the total integrated flux of the CO (1-0) map inside the Band 3 FoV (541 ± 27 Jy km s $^{-1}$). This implies that, assuming as an extreme case that [C I] (1-0) emission traces similar structures seen in CO (1-0) emission, the [C I] (1-0) total flux inside the Band 3 FoV should be 1780 ± 356 Jy km s $^{-1}$. We

regard this value as the [C I] (1-0) total flux of our data in order to estimate the amount of missing flux. The [C I] (1-0) *Herschel*/SPIRE single-dish flux is 2300 ± 370 Jy km s $^{-1}$ (Kamenetzky et al. 2016), for which we assumed a systematic flux uncertainty of 16% (Rosenberg et al. 2015). This indicates that the recovered [C I] (1-0) flux is 77 ± 20 %, which is consistent with the recovered CO (1-0) flux of 79 ± 9 % (NRAO 12m flux = 686 ± 69 Jy km s $^{-1}$; Garay et al. 1993). If we assume the opposite extreme case that the SPIRE [C I] (1-0) total flux comes from an area within the Band 8 FoV of $\sim 13''$ 0, the recovered [C I] (1-0) flux will be 67 ± 17 %. This is on the order of the absolute flux calibration uncertainties between the two observations. Thus, throughout this paper, we do not consider that the missing flux affects our analysis and conclusion. We note that the step calculating the expected total [C I] (1-0) flux inside the Band 3 FoV carries a significant uncertainty.

We show the radial flux distributions of CO (1-0), [C I] (1-0), and 609 μ m continuum in Figure 1d. We define the peak position of the CO (1-0) emission as the centre. We found that the apparent disk size is different among the gas mass tracers (CO > [C I] > dust). Recent high-resolution CO and dust observations toward the nearby merging (U)LIRGs have revealed that 850 μ m dust continuum distribution is typically more compact than the low- J CO flux distribution in nearby (U)LIRGs (e.g., Wilson et al. 2008; Sakamoto et al. 2014; Saito et al. 2015, 2017). Those differences may be driven by a combination of temperature, optical depth, and abundance gradients, which can be revealed through multiple frequency and line observations.

3.2 Pixel-by-pixel Comparison

We calculate luminosities of both lines (L'_{line}) in units of K km s $^{-1}$ pc 2 by using the following equation (Solomon, & Vanden Bout 2005);

$$L'_{\text{line}} = 3.25 \times 10^7 S_{\text{line}} \Delta v \nu_{\text{obs}}^{-2} D_L^2 (1+z)^{-3} \quad (1)$$

where $S_{\text{line}} \Delta v$ is the velocity-integrated flux of a line in Jy km s $^{-1}$, ν_{obs} is the observed frequency of the line in GHz, D_L is the source luminosity distance in Mpc, and z is the source redshift. The continuum luminosity at the frequency of ν (L_ν) in units of erg s $^{-1}$ Hz $^{-1}$ is calculated via;

$$L_\nu = 1.20 \times 10^{27} S_{\nu_{\text{obs}}} D_L^2 (1+z)^{-3} \quad (2)$$

where S_ν is the observed continuum flux density in Jy.

Pixel-by-pixel comparisons between CO and [C I] luminosities and between 609 μ m dust continuum and [C I] luminosities are shown in Figures 2a and 2b, respectively, both of which show a clear correlation. We would like to remind the readers that the pixel size is 0''.18 (~ 65 pc) and correlates across the beam (~ 300 pc). Although our sensitivity limits (grey shaded areas) look sufficient to evaluate the correlation strength, the scatter seems to hit the [C I] sensitivity limit (Figures 2a).

To further investigate this, we compare the [C I]/CO luminosity ratio against the CO luminosity pixel-by-pixel (Figure 2c). Now it becomes apparent that the current [C I] sensitivity is limiting the completeness at $\log(L'_{\text{CO(1-0)}}/(\text{K km s}^{-1} \text{ pc}^2)) < 6.0$. This is also seen in the turnover of the

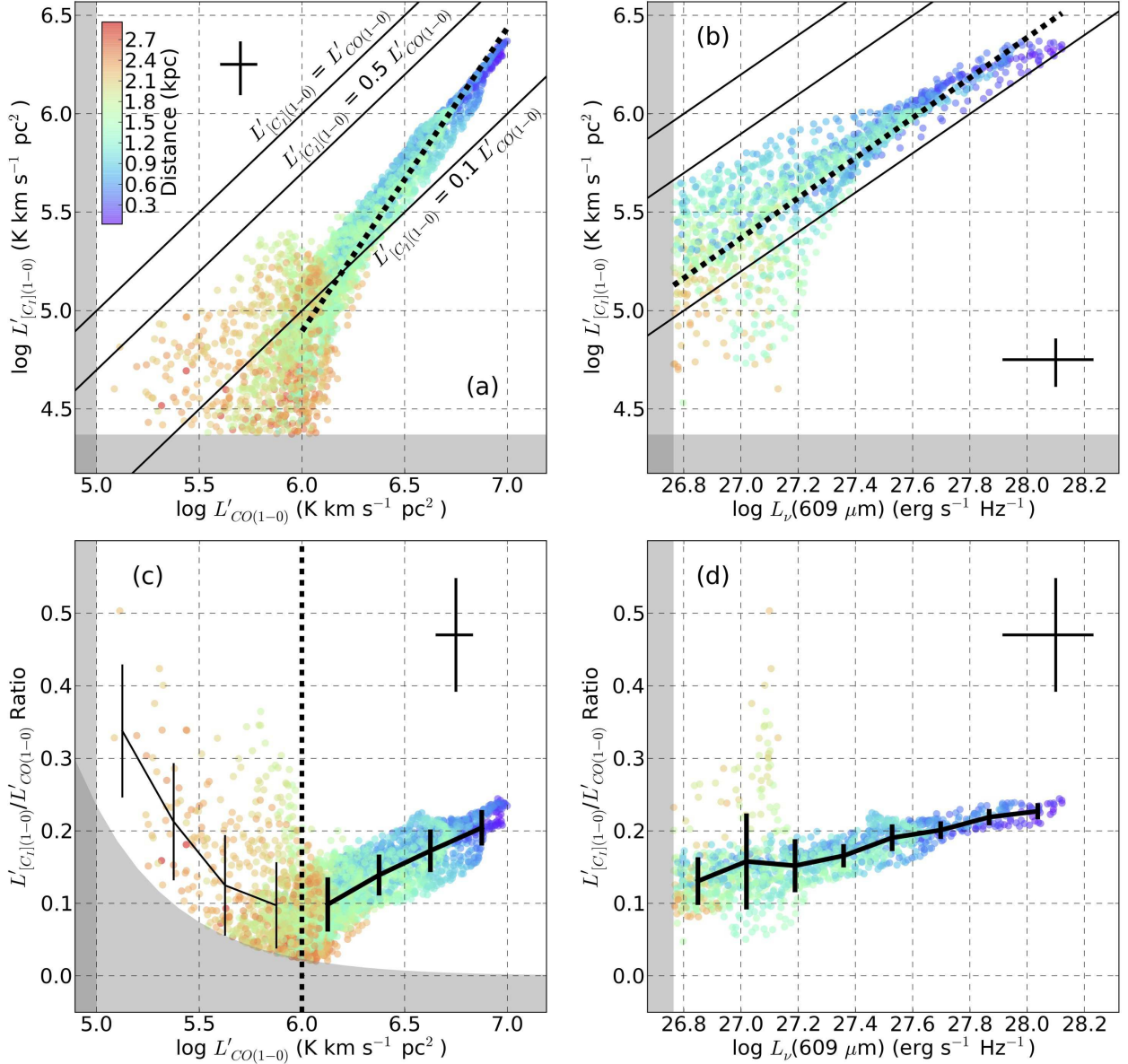


Figure 2. (a) Pixel-by-pixel comparison between [C I] (1–0) and CO (1–0) luminosities toward IRAS F18293-3413. The color scale corresponds to distance from centre. Typical error bars including the statistical error and the systematic flux error are shown in the top left corner. Grey areas have less than 3σ sensitivity. Three black solid lines indicate linear relations for [C I]/CO = 1.0, 0.5, and 0.1. The dashed black line shows the best fit relation to the data points with $\log(L'_{CO(1-0)} \text{ (K km s}^{-1} \text{ pc}^2)^{-1}) > 6.0$ (see text). (b) Pixel-by-pixel comparison between [C I] (1–0) and 609 μm luminosities. The three black solid lines are the same as those in panel (a) when $\log L_{\nu(609 \mu\text{m})} = 20.8 + \log L'_{CO(1-0)}$. The dashed black line shows the best fit relation to the data points. (c) Pixel-by-pixel comparison between [C I]-to-CO luminosity ratio and CO (1–0) luminosity. A dashed vertical line presents the completeness limit of $\log(L'_{CO(1-0)} \text{ (K km s}^{-1} \text{ pc}^2)^{-1}) = 6.0$. Binned distributions showing the median with the standard deviation at each bin are shown as black solid lines. The data points are divided into 8 equally-spaced bins. (d) Pixel-by-pixel comparison between [C I]-to-CO luminosity ratio and 609 μm luminosity. The very high ratios seen in the lower luminosity regimes mainly come from pixels which satisfies (1) low signal-to-noise CO (1–0) and (2) located at the edge of the Band 8 FoV.

binned ratio distribution around $\log(L'_{CO(1-0)}/(\text{K km s}^{-1} \text{ pc}^2)) = 6.0$. Thus, when comparing [C I] with CO, we decided to use data points with high completeness hereafter (i.e., $\log(L'_{CO(1-0)}/(\text{K km s}^{-1} \text{ pc}^2)) > 6.0$), which biases our results to brighter pixels, although we are able to use $\gtrsim 80\%$ of pixels inside the Band 8 FoV. Deeper [C I] data is required to overcome this limitation. In the case of the [C I]/CO lu-

minosity ratio against 609 μm dust continuum luminosity (Figure 2d), we do not consider the completeness limit described above as one of the advantages of this comparison is to remove the correlation between the x and y axes, though the limited [C I] sensitivity is still an issue especially the lower luminosity regime.

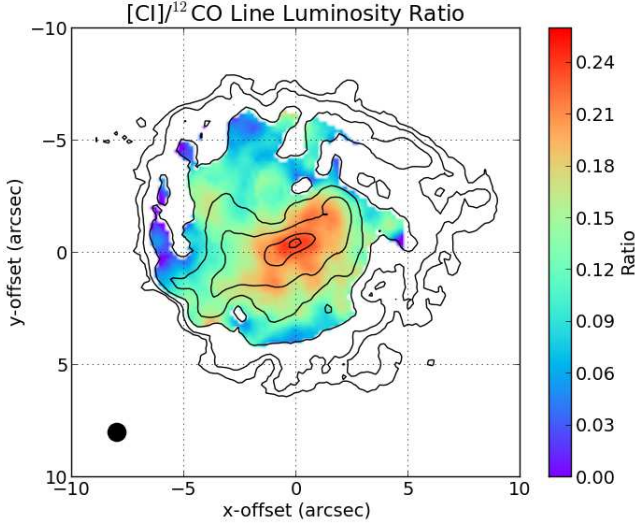


Figure 3. A map of the [C I] (1–0)/CO (1–0) line luminosity ratio of IRAS F18293-3413. All pixels lower than $\log L'_{\text{CO}(1-0)} = 6.0 \text{ K km s}^{-1} \text{ pc}^2$ are clipped (see text for details). The convolved synthesized beam is shown in the lower left corner. The contours are the same as in Figure 1a.

3.2.1 [C I] (1–0) vs. CO (1–0)

We carried out a linear fitting to the [C I] (1–0) and CO (1–0) data points with high completeness in Figure 2a, and we found a superlinear relation;

$$\log_{10} L'_{[\text{C I}](1-0)} = (1.54 \pm 0.02) \log_{10} L'_{\text{CO}(1-0)} - (4.35 \pm 0.15). \quad (3)$$

This is also seen in the positive slope in Figure 2c.

In Figure 3, we show a map of the [C I]/CO line luminosity ratio map above the completeness limit. This is the first 300-pc scale view of the [C I]/CO line ratio toward the whole gas disk of a LIRG. There is a tendency that the central region has higher ratio (~ 0.24) and the outer parts of the galaxy show lower values (~ 0.1). The ratio variation in IRAS F18293-3413 is within the variation of single-dish global values found for extragalactic objects (0.2 ± 0.2 ; Gerin, & Phillips 2000; Jiao et al. 2017).

We show the line luminosity ratio histogram and a best-fit Gaussian to the distribution in Figure 4a. The ratio distribution is well represented by a single Gaussian with $\mu = 0.16$ and $\sigma = 0.04$. When the distribution is weighted by the [C I] (1–0) luminosity, i.e., a histogram showing total [C I] (1–0) luminosity at a given [C I]/CO ratio bin, the shape remains similar to a single Gaussian with the peak slightly moving to the right (Figure 4c; $\mu = 0.18$ and $\sigma = 0.04$). This indicates that the [C I] (1–0) intensity mainly come from higher ratio pixels, which is consistent with the impression of Figure 3 what the bright centre shows higher ratios.

A similar radial trend was reported toward the circumnuclear disk of the nearby Seyfert galaxy NGC 1808 (Salak et al. 2019) and the central kpc of the nearby starburst galaxy NGC 253 (Krips et al. 2016) using well-resolved datasets with $\lesssim 100 \text{ pc}$ resolution. They basically found regions with brighter CO emission tend to show higher [C I] (1–0)/CO (1–0) ratios, that is, a superlinear relation in

the [C I] (1–0) and CO (1–0) scatter plot as we found in IRAS F18293-3413.

The superlinear relation seen in our 300-pc scale measurement, as well as by Krips et al. (2016) and Salak et al. (2019), seems inconsistent with the moderately spatially-resolved measurements of nearby normal galaxies and the global measurements of (U)LIRGs, both of which exhibit a linear relationship (Jiao et al. 2019). However, Jiao et al. (2019) fitted the (U)LIRG data points independently of the data points for nearby normal galaxies using a fixed slope of unity (dashed-dotted blue line of their Figure 3), which is consistent with their earlier work which presented an almost linear fit of their (U)LIRG sample with a free slope (Jiao et al. 2017). They did the same fitting for the nearby galaxy data points (dashed-dotted red line of Jiao et al. 2019), where the relation is offset to lower [C I]/CO ratios compared to the fitted linear relation for (U)LIRGs. This implies if one simultaneously fits all their data points with a free slope, the derived slope will be larger than unity. Thus, the superlinear relation we derived for IRAS F18293-3413 is consistent with what Jiao et al. (2019) found.

We note that the integrated luminosities of IRAS F18293-3413 within the Band 8 FoV ($L'_{\text{CO}(1-0)} \sim 10^{9.8} \text{ K km s}^{-1} \text{ pc}^2$ and $L'_{[\text{C I}](1-0)} \sim 10^{9.0} \text{ K km s}^{-1} \text{ pc}^2$) are consistent within the scatter of the CO (1–0) vs. [C I] (1–0) luminosity plot for nearby (U)LIRGs (Jiao et al. 2017).

3.2.2 [C I] (1–0) vs. Cold Dust

We fit the CI and $609 \mu\text{m}$ dust data points (Figure 2b) in the same way as described in the previous section, and found a nearly linear relation in contrast to the [C I] (1–0) and CO (1–0) relation;

$$\log_{10} L'_{[\text{C I}](1-0)} = (1.02 \pm 0.02) \log_{10} L_{\nu}(609\mu\text{m}) - (22.12 \pm 0.58). \quad (4)$$

The line luminosities correlate well with the dust continuum luminosity at brighter pixels, although the scatter becomes larger at the fainter dust luminosity regime. We show a comparison between the [C I]/CO luminosity ratio against the dust continuum luminosity in Figure 2d, and found a position correlation similar to that in Figure 2c.

We plot [C I]/dust luminosity ratio histograms in Figures 4b and 4d. The x-axis is scaled by $10^{20.8}$ to make a comparison with [C I]/CO ratio histograms easier. The [C I]/dust ratio histograms ($\mu = 0.15$ and $\sigma = 0.03$) have a similar shape to (or are very slightly narrower than) the [C I]/CO ratio histograms. However, in contrast to the [C I]/CO ratio, the weighted [C I]/dust histogram gives similar the μ and σ as the unweighted histogram, implying that both the bright centre and the fainter outer region show a similar [C I]/dust ratio in general. The extreme values (>0.25 or <0.07) come from a small number of low signal-to-noise pixels.

In summary, we find that the [C I] (1–0) line is surprisingly well correlated with the $609 \mu\text{m}$ dust continuum, but much less tracing the CO (1–0) line at 300 pc scale in this galaxy.

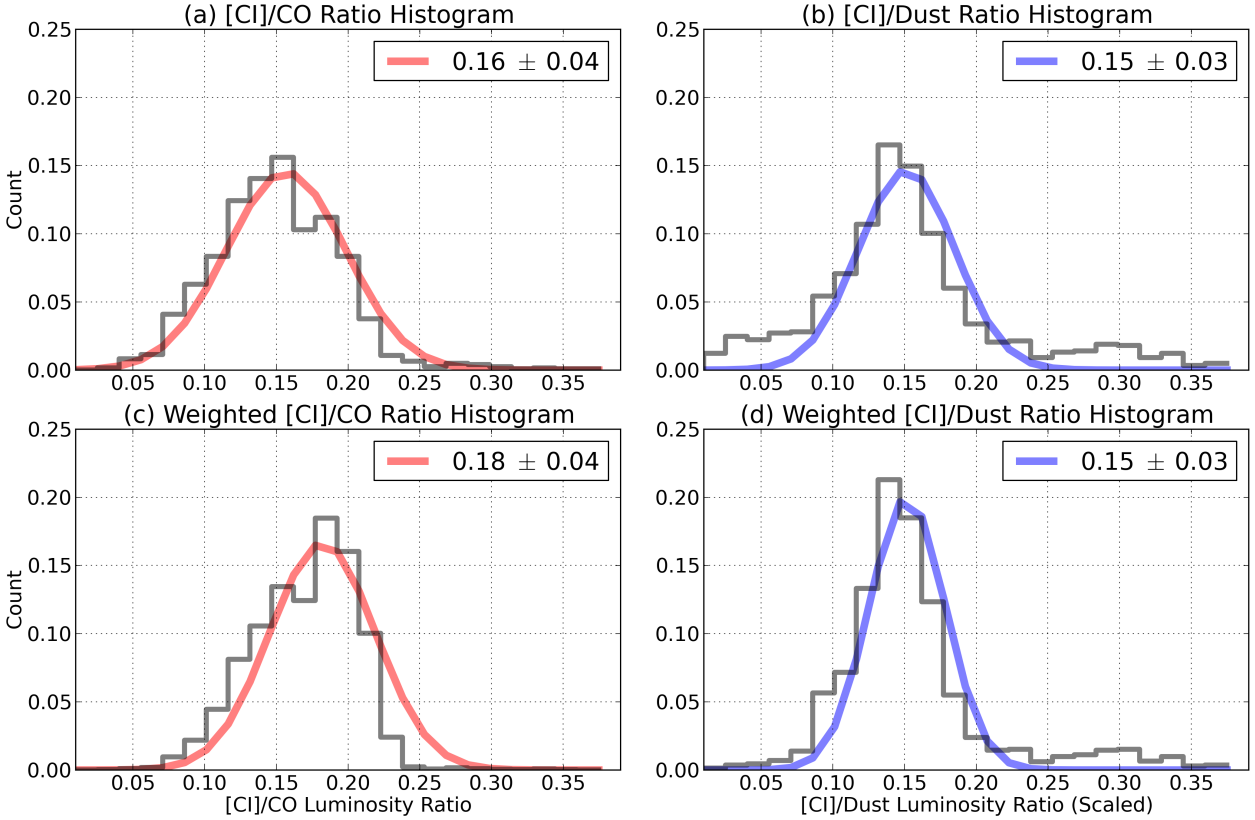


Figure 4. (a) Histogram of the [C I] (1–0)/CO (1–0) line luminosity ratio. A best-fit Gaussian fit to the histogram is shown by the coloured bins. (b) Histogram of the [C I] (1–0)/dust continuum luminosity ratio scaled by $10^{20.8}$ assuming $\log L_{\nu}(609 \mu\text{m}) = 20.8 + \log L'_{\text{CO}(1-0)}$. (c/d) Same as panel (a/b), but histograms are weighted by the [C I] (1–0) luminosity.

4 DISCUSSION

Here we discuss the origin of the slope of the correlations between different gas mass tracers presented in Section 3. Then, we derive the line luminosity to H_2 gas mass conversion factor (α_{line}) for CO (1–0) and [C I] (1–0) using gas masses based on the $609 \mu\text{m}$ dust continuum. Finally, we discuss which physical parameters are required to reproduce the derived $\alpha_{[\text{C I}](1-0)}$ based on non local thermodynamic equilibrium (non-LTE) radiative transfer modeling.

4.1 Origin of the Slopes

An observed luminosity ratio between two emission lines is a result of the combination of line opacity and gas physical properties. According to the radiative transfer equation, the observed line intensity in units of brightness temperature (T_{line}) can be expressed as,

$$T_{\text{line}} = \eta_{\text{bf}} \left(\frac{h\nu_{\text{obs}}/k}{e^{h\nu_{\text{obs}}/kT_{\text{ex}}} - 1} - \frac{h\nu_{\text{obs}}/k}{e^{h\nu_{\text{obs}}/kT_{\text{cmb}}} - 1} \right) (1 - e^{-\tau_{\text{line}}}), \quad (5)$$

where η_{bf} is the beam filling factor, h is Planck's constant, k is Boltzmann's constant, T_{ex} is the excitation temperature of the line, T_{cmb} is the cosmic microwave background temperature ($= 2.73 \text{ K}$), and τ_{line} is the line opacity.

If we assume two lines (i.e., CO (1–0) and [C I] (1–0) lines) have a very similar or the exactly same beam filling factor ($\eta_{\text{bf,CO}(1-0)} \approx \eta_{\text{bf,[C I}](1-0)}$), the line luminosity ratio

(R) becomes,

$$R = \frac{J(T_{\text{ex,[C I}](1-0)}) - J(T_{\text{cmb}})}{J(T_{\text{ex,CO}(1-0)}) - J(T_{\text{cmb}})} \frac{1 - e^{-\tau_{[\text{C I}](1-0)}}}{1 - e^{-\tau_{\text{CO}(1-0)}}}, \quad (6)$$

where $J = (h\nu_{\text{obs}}/k)(e^{h\nu_{\text{obs}}/kT} - 1)$. This is the same equation presented in Salak et al. (2019).

According to the equation, there are three different ways to increase R : (1) increase temperature when $T_{\text{ex,CO}(1-0)} \approx T_{\text{ex,[C I}](1-0)}$, (2) increase $\tau_{[\text{C I}](1-0)}$ when $\tau_{\text{CO}(1-0)} \gg 1$, and/or (3) decrease $\tau_{\text{CO}(1-0)}$ when $\tau_{[\text{C I}](1-0)} \ll 1$.

(1) Based on the non-LTE radiative transfer calculation done by Salak et al. (2019), the assumption that both lines are nearly thermalized is reasonable ($T_{\text{ex,CO}(1-0)} \approx T_{\text{ex,[C I}](1-0)} \approx T_{\text{kin}}$, where T_{kin} is the gas kinetic temperature) under typical molecular gas conditions found in nearby (U)LIRGs (e.g., Saito et al. 2017; Sliwa et al. 2017), i.e., relatively warm and moderately dense condition ($T_{\text{kin}} \sim 40\text{--}80 \text{ K}$ and $n_{\text{H}_2} \sim 10^{3-4} \text{ cm}^{-3}$). In this case, R monotonically increases as T_{kin} increases. Since the central part of galaxies typically shows a stronger interstellar radiation field that is efficiently heating the surrounding material, the expected radial T gradient results in a radial R gradient and thus a superlinear relation. This scenario is supported by Jiao et al. (2019), which show that a marginally resolved radial [C I] (2–1)/[C I] (1–0) gradient in the nearby edge-on starburst galaxy M82.

(2) If T_{kin} is almost constant (or has a negligible radial

gradient) across the molecular gas disk of IRAS F18293-3413, the observed radial R gradient can be only reproduced by varying the line opacities. At first, we assume $\tau_{\text{CO}(1-0)} \gg 1$. In order to reproduce the observed radial R gradient from 0.25 to 0.1, $\tau_{[\text{C I}](1-0)}$ should be moderate to optically thin across the disk (between 0.4 and 0.1). This is consistent with the fact that [C I] (1–0) linearly correlates with optically-thin dust continuum emission assuming $T_{\text{ex},[\text{C I}](1-0)} \approx T_{\text{dust}}$. Note that many previous extragalactic works also argued that the [C I] (1–0) line is optically-thin to moderately thin based on radiative transfer analysis (e.g., Israel et al. 2015; Krips et al. 2016).

(3) The another possibility is a variation of $\tau_{\text{CO}(1-0)}$. If $\tau_{[\text{C I}](1-0)}$ is optically-thin and almost constant radially, $\tau_{\text{CO}(1-0)} \lesssim 1$ around the centre of IRAS F18293-3413 can explain the superlinear relation. However, galaxy centres, especially (U)LIRG nuclei, typically exhibit higher H_2 column density, implying that $\tau_{\text{CO}(1-0)} \lesssim 1$ at the centre may be unrealistic.

We cannot reject any of these three possibilities for now, mainly because of the lack of an independent optically-thin molecular gas mass tracer (e.g., ^{13}CO lines) and constraints on the excitation condition of the CO and [C I] lines at the same high-resolution scale.

4.2 Measuring Conversion Factor Distributions

As discussed in many previous atomic carbon studies for more than two decades (see Section 1), extragalactic astronomers have tried to utilize the [C I] (1–0) line emission as a tracer of total molecular gas mass by taking advantage of its low to moderate optical depth and the simple three energy level system of the [C I] lines. However, we do not exactly know the excitation condition and the optical depth of the [C I] (1–0) line because of the lack of [C I] (2–1) data at the same spatial resolution. Thus, in this section we utilize the optically-thin $609\mu\text{m}$ dust continuum as a gold standard molecular gas mass estimator following the prescription described in Scoville et al. (2016), and then calculate conversion factors. Plausibility of the derived conversion factors and a comparison with previous works will be presented in the next section.

To derive the total molecular gas mass (i.e., H_2+He) in units of M_\odot we use the equations 6 and 16 of Scoville et al. (2016);

$$M_{\text{H}_2} = 1.78 S_{\nu_{\text{obs}}} (1+z)^{-4.8} \left(\frac{\nu_{850\mu\text{m}}}{\nu_{\text{obs}}} \right)^{3.8} D_{\text{L}}^2 \times \left(\frac{6.7 \times 10^{19}}{\alpha_{850\mu\text{m}}} \right) \frac{\Gamma_0}{\Gamma_{\text{RJ}}} 10^{10}, \quad (7)$$

where $S_{\nu_{\text{obs}}}$ is the observed flux densities in units of mJy, D_{L} is the luminosity distance in Gpc, α_{850} is the conversion factor from $850\mu\text{m}$ continuum to total molecular gas mass assuming $T_{\text{dust}} = 25$ K. This is similar to $T_{\text{ex},\text{CO}(1-0)}$ and $T_{\text{ex},[\text{C I}](1-0)}$ under typical (U)LIRG conditions (Salak et al. 2019). We use $\alpha_{850\mu\text{m}} = 6.7 \times 10^{19} \text{ erg s}^{-1} \text{ Hz}^{-1} M_\odot^{-1}$, which is a calibrated value for local star-forming galaxies, (U)LIRGs, and high- z submillimeter galaxies. Γ_{RJ} is given by,

$$\Gamma_{\text{RJ}}(T_{\text{dust}}, \nu_{\text{obs}}, z) = \frac{h\nu_{\text{obs}}(1+z)/kT_{\text{dust}}}{e^{h\nu_{\text{obs}}(1+z)/kT_{\text{dust}}} - 1}, \quad (8)$$

and $\Gamma_0 = \Gamma_{\text{RJ}}(T_{\text{dust}}, \nu_{850\mu\text{m}}, 0)$. We note that we assume $T_{\text{dust}} = 25$ K. This is consistent with a grey body fitting to the FIR spectral energy distribution of nearby (U)LIRGs (33.2 ± 6.2 K; U et al. 2012).

Radial distribution of the derived molecular gas masses divided by the CO (1–0) and [C I] (1–0) luminosities, i.e., $\alpha_{\text{CO}(1-0)}$ and $\alpha_{[\text{C I}](1-0)}$, respectively, are shown in Figure 5. The distributions are relatively flat with a peak at the centre. Note that flatter radial α_{CO} distributions are reported in nearby spiral galaxies and the nearby LIRG NGC 1614 (Sandstrom et al. 2013; Saito et al. 2017). The dispersions seen at large radii are due to low signal-to-noise ratios of the dust continuum data, which are already seen in the weighted and unweighted histograms in Figures 4.

The median $\alpha_{\text{CO}(1-0)}$ for IRAS F18293-3413 is $3.5 M_\odot (\text{K km s}^{-1} \text{ pc}^2)^{-1}$. This $\alpha_{\text{CO}(1-0)}$ is between the empirical value for the Milky Way (~ 4.3 ; Bolatto et al. 2013) and that of nearby (U)LIRGs (~ 0.8 ; Downes, & Solomon 1998). The 16% and 84% percentiles of the $\alpha_{\text{CO}(1-0)}$ distribution is 2.2 and $5.4 M_\odot (\text{K km s}^{-1} \text{ pc}^2)^{-1}$, respectively, and thus most of the pixels show $\alpha_{\text{CO}(1-0)}$ comparable or slightly lower than the Milky Way value.

We found the $\alpha_{[\text{C I}](1-0)}$ distribution is relatively flat across the molecular gas disk of IRAS F18293-3413 with a median = $20.7 M_\odot (\text{K km s}^{-1} \text{ pc}^2)^{-1}$, 16% percentile = $15.8 M_\odot (\text{K km s}^{-1} \text{ pc}^2)^{-1}$, and 84% percentile = $29.9 M_\odot (\text{K km s}^{-1} \text{ pc}^2)^{-1}$, which are larger than $\alpha_{\text{CO}(1-0)}$ by an order of magnitude. The flat radial $\alpha_{[\text{C I}](1-0)}$ distribution is a natural consequence of the linear relation between [C I] and dust (Figure 2b). Israel et al. (2015) reported that the global $\alpha_{[\text{C I}](1-0)}$ values are roughly 10 times larger than the global $\alpha_{\text{CO}(1-0)}$ for nearby (U)LIRGs, which support our spatially-resolved measurements here.

Conversion factors derived above are based on the gas masses with a fixed $\alpha_{850\mu\text{m}}$ of $6.7 \times 10^{19} \text{ erg s}^{-1} \text{ Hz}^{-1} M_\odot$ (Scoville et al. 2016). Here we briefly discuss how the results change when applying variable $\alpha_{850\mu\text{m}}$. We use a linear relation proposed by (i.e., luminosity-dependent $\alpha_{850\mu\text{m}}$; Hughes et al. 2017), which can be written as,

$$\log_{10} M_{\text{H}_2} = (0.92 \pm 0.02) \log_{10} L_{\nu_{850}} - (17.31 \pm 0.59) \quad (9)$$

where $L_{\nu_{850}}$ is the continuum luminosity at $850\mu\text{m}$. We use the exactly same parameters used in Equation 8 to convert the observed $609\mu\text{m}$ flux to the $850\mu\text{m}$ flux.

The median value is $4.1 \times 10^{19} \text{ erg s}^{-1} \text{ Hz}^{-1} M_\odot$, which makes the resultant $\alpha_{\text{CO}(1-0)}$ and $\alpha_{[\text{C I}](1-0)}$ larger than values seen in Figure 5 by $\sim 50\%$. The radial trends seen in Figure 5 does not change, because the derived $\alpha_{850\mu\text{m}}$ is almost constant across the disk of IRAS F18293-3413 (maximum and minimum are 3.8×10^{19} and $4.8 \times 10^{19} \text{ erg s}^{-1} \text{ Hz}^{-1} M_\odot$, respectively).

4.3 Physical Properties of the [C I] (1–0)-emitting ISM in IRAS F18293-3413

In this section, we discuss possible physical conditions of the ISM emitting [C I] (1–0) line emission which can reproduce the derived $\alpha_{[\text{C I}](1-0)}$ values. We follow the optically-thin prescription described in Papadopoulos et al. (2004) (see also Alaghband-Zadeh et al. 2013).

To derive the total molecular gas mass using the [C I] (1–

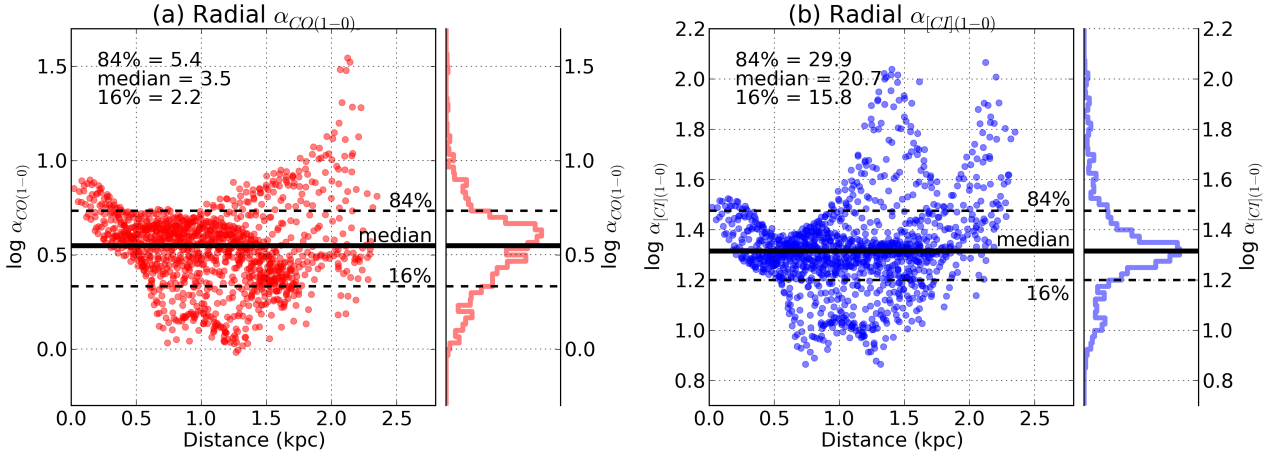


Figure 5. (a) Radial $\alpha_{\text{CO}(1-0)}$ ($= M_{\text{H}_2}/L'_{\text{CO}(1-0)}$) distribution and histogram. The solid and two dashed black lines illustrate the 16th, 50th (median), and 84th percentiles. (b) Same as panel (a), but for $\alpha_{[\text{C I}](1-0)}$ ($= M_{\text{H}_2}/L'_{[\text{C I}](1-0)}$).

0) line, we use the equation;

$$M_{\text{H}_2} = 1375.8 \frac{D_L^2}{1+z} \left(\frac{X_{\text{C I}}}{10^{-5}} \right)^{-1} \times \left(\frac{A_{10}}{10^{-7} \text{ s}^{-1}} \right)^{-1} Q_{10}^{-1} \frac{S_{\text{line}} \Delta v}{\text{Jy km s}^{-1}} \quad (10)$$

where, A_{10} is the Einstein coefficient ($= 7.93 \times 10^{-8} \text{ s}^{-1}$), $X_{\text{C I}}$ is the CI abundance relative to H_2 , and Q_{10} is the [C I] (1–0) excitation factor.

By substituting equation 1 for equation 10, $\alpha_{[\text{C I}](1-0)}$ can be expressed as,

$$\alpha_{[\text{C I}](1-0)} \equiv \frac{M_{\text{H}_2}}{L'_{[\text{C I}](1-0)}} = 3.357 \gamma_{\text{obs}}^2 (1+z)^2 X_{\text{C I}}^{-1} Q_{10}^{-1}, \quad (11)$$

where $X_{\text{C I}}$ is the abundance of atomic carbon relative to H_2 and Q_{10} is the [C I] (1–0) partition function. According to the equation, $\alpha_{[\text{C I}](1-0)}$ is simply inversely proportional to Q_{10} and $X_{\text{C I}}$, while both cannot be constrained by the current dataset. Thus, we explore Q_{10} and $X_{\text{C I}}$ values in order to reproduce the derived $\alpha_{[\text{C I}](1-0)}$.

In Figure 6, we plot $\alpha_{[\text{C I}](1-0)}$ values within reasonable ranges of Q_{10} and $X_{\text{C I}}$. We found that the derived $\alpha_{[\text{C I}](1-0)}$ for IRAS F18293-3413 can be reproduced within $Q_{10} = 0.35$ –0.50, and $X_{\text{C I}} = (0.8$ – $2.3) \times 10^{-5}$.

In the case of optically-thin [C I] emission and weak radiation limit (i.e., $T_{\text{kin}} \gg$ background temperature $\sim 2.73 \text{ K}$), we can estimate $Q_{10}(T_{\text{kin}}, n)$ by using Equations (A21) and (A25) of Papadopoulos et al. (2004). Based on a non-LTE Q_{10} grid in the n – T_{kin} plane presented in Figure 3c in Jiao et al. (2017), Q_{10} varies from 0.35 to 0.50 for the typical molecular gas conditions observed in nearby (U)LIRGs ($n = 10^3$ – 10^4 cm^{-3} and $T_{\text{kin}} = 20$ – 50 K). From Figure 6, under the non-LTE assumption, the typical molecular gas conditions in nearby (U)LIRGs naturally explain the derived $\alpha_{[\text{C I}](1-0)}$ when $X_{\text{C I}} = (0.8$ – $2.3) \times 10^{-5}$.

$X_{\text{C I}}$ is observationally known to vary from 4 – 8×10^{-5} (high-redshift SMGs and quasars; Alaghband-Zadeh et al. 2013; Walter et al. 2011) to 4×10^{-5} (nearby galaxies; Israel, & Baas 2001, 2003), and to 2×10^{-5} (Galactic star-forming regions; Frerking et al. 1989) with large systematic

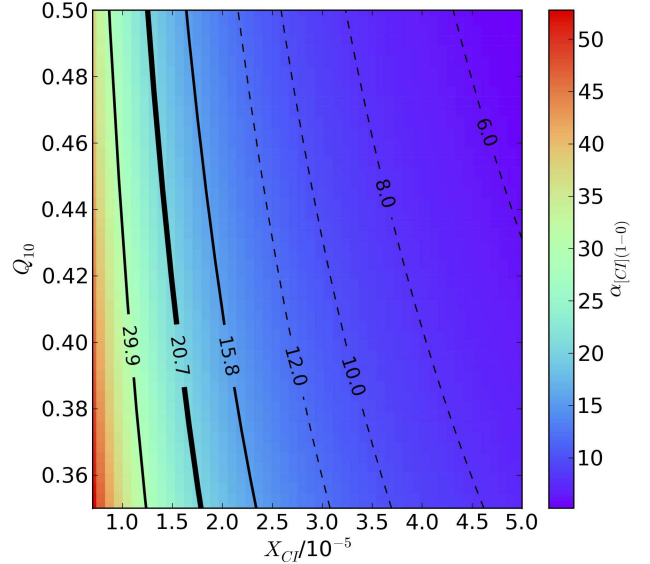


Figure 6. The $\alpha_{[\text{C I}](1-0)}$ distribution in the Q_{10} – $X_{\text{C I}}$ plane. The solid lines highlight the 16%, 50%, and 84% percentiles of the derived $\alpha_{[\text{C I}](1-0)}$ distribution for IRAS F18293-3413. The dashed lines highlight other $\alpha_{[\text{C I}](1-0)}$ values for reference.

uncertainties depending on the method to estimate the H_2 column density. Recently, Valentino et al. (2018) reported 1.6 – 1.9×10^{-5} for main-sequence galaxies at $z = 1$ – 2 , which is consistent with or lower than the previous studies. There seems to be a trend that active objects show higher $X_{\text{C I}}$. The $\alpha_{[\text{C I}](1-0)}$ value decreases as $X_{\text{C I}}$ increases with a negligible relative influence of Q_{10} (Figure 6), so that active objects showing higher $X_{\text{C I}}$ imply lower $\alpha_{[\text{C I}](1-0)}$ (~ 5 – $10 M_{\odot} (\text{K km s}^{-1} \text{ pc}^2)^{-1}$). This is the same trend as for $\alpha_{\text{CO}(1-0)}$ which shows a systematic variation from the Milky Way ($\sim 4.3 M_{\odot} (\text{K km s}^{-1} \text{ pc}^2)^{-1}$) to (U)LIRGs ($\sim 0.8 M_{\odot} (\text{K km s}^{-1} \text{ pc}^2)^{-1}$).

Heintz & Watson (2020) found that $\alpha_{[\text{C I}](1-0)}$ monotonically decrease as the metallicity increases in absorption-selected high-redshift galaxies. Since $X_{\text{C I}}$ is considered to be mainly driven by metallicity (Glover, & Clark 2016), this

study supports the expected relation between $\alpha_{[\text{C I}](1-0)}$ and $X_{\text{C I}}$ (see also Crocker et al. 2019).

Moreover, one may expect that more intense star-forming environments show higher $X_{\text{C I}}$ due to large cosmic ray (CR) flux and strong UV radiation (Papadopoulos et al. 2004). This suggests a possible CR-driven radial $X_{\text{C I}}$ distribution in the disk of galaxies, leading to lower $\alpha_{[\text{C I}](1-0)}$ for the centre of IRAS F18293-3413. Thus, the radial $\alpha_{[\text{C I}](1-0)}$ distribution may become flatter, once one can estimate the impact of CR on the spatial $X_{\text{C I}}$ distribution.

The assumed [C I] line physical parameters significantly affect spatially-resolved molecular gas mass measurements as briefly described above. In order to constrain both Q_{10} and $X_{\text{C I}}$ distributions, multi-CO radiative transfer analysis and the higher fine structure of atomic carbon line, [C I] (2–1), are needed.

5 CONCLUSIONS

In this paper, we present high-quality ALMA observations of [C I] (1–0) CO (1–0), and 609 μm dust continuum emission toward the nearby LIRG IRAS F18293-3413 at 300-pc ($\sim 0.8''$) resolution, providing spatially-resolved measurements of both lines and the continuum for the whole gas disk of a single galaxy with sufficient resolution and sensitivity. We detect both lines with significant signal-to-noise to characterize their spatial distributions. The [C I]/CO line luminosity ratio is complete above a CO (1–0) luminosity = $10^6 \text{ K km s}^{-1} \text{ pc}^2$, while it is sufficient to measure radial trends up to 2.5 kpc distance from the centre. Within this distance, we also detect the continuum emission.

We find that the [C I] (1–0) line traces structures detected in CO (1–0) and 609 μm dust emission, and the [C I] and dust flux distributions are apparently comparable or slightly more compact than CO (1–0). However, a pixel-by-pixel comparison revealed that there is a superlinear relation (slope = 1.54 ± 0.02) between CI and CO luminosities and a linear relation between CI and 609 μm dust luminosities. Those relations can be explained by radially varying excitation temperature and/or line opacity gradients.

The [C I] (1–0)/CO (1–0) ratio histogram is well fitted by a single Gaussian component with $\mu = 0.16$ and $\sigma = 0.04$, and the scaled [C I] (1–0)/dust ratio histogram shows a similar distribution. However, the luminosity-weighted [C I] (1–0)/CO (1–0) ratio histogram shows an offset from a Gaussian due to the high line ratios around the centre of IRAS F18293-3413.

We convert the 609 μm dust emission to the molecular gas mass in order to calculate radial distributions of the CO (1–0)-to- H_2 ($\alpha_{\text{CO}(1-0)}$) and [C I] (1–0)-to- H_2 ($\alpha_{[\text{C I}](1-0)}$) conversion factors within the disk of IRAS F18293-3413. The derived conversion factors are relatively constant values (median $\alpha_{\text{CO}(1-0)} = 3.5$ and $\alpha_{[\text{C I}](1-0)} = 20.7 M_{\odot} (\text{K km s}^{-1} \text{ pc}^2)^{-1}$) across the disk with some dispersions at larger distance from the centre which are mainly driven by low signal-to-noise data points. A non-LTE calculation yields that typical molecular gas properties ($n_{\text{H}_2} = 10^{3-4} \text{ cm}^{-3}$, $T_{\text{kin}} = 40\text{--}50 \text{ K}$, and $X_{\text{C I}} = (0.8\text{--}2.3) \times 10^{-5}$) can naturally explain the derived $\alpha_{[\text{C I}](1-0)}$.

The [C I] (1–0) line can be used to trace the molecular gas kinematics and infer flux distribution of CO (1–0) and

dust emission within the gas disk of galaxies. However, a careful treatment on the gas physical properties (e.g., radial slope of gas temperature and C I abundance) is required in order to measure H_2 gas mass distribution in galaxies using a single [C I] line. Otherwise, a [C I] line is not a good molecular gas estimator in a spatially resolved manner.

ACKNOWLEDGEMENTS

The authors thanks an anonymous referee for comments that significantly improved the contents of this paper. T.S., D.L. and E.S. acknowledge funding from the European Research Council (ERC) under the European Union’s Horizon 2020 research and innovation programme (grant agreement No. 694343). Y.A. acknowledges financial support by NSFC grant 11933011. This paper makes use of the following ALMA data: ADS/JAO.ALMA#2015.1.01191.S and ADS/JAO.ALMA#2018.1.00994.S. ALMA is a partnership of ESO (representing its member states), NSF (USA) and NINS (Japan), together with NRC (Canada), MOST and ASIAA (Taiwan), and KASI (Republic of Korea), in cooperation with the Republic of Chile. The Joint ALMA Observatory is operated by ESO, AUI/NRAO and NAOJ. This research has made use of the NASA/IPAC Extragalactic Database (NED) which is operated by the Jet Propulsion Laboratory, California Institute of Technology, under contract with the National Aeronautics and Space Administration. This research made use of Astropy, a community-developed core Python package for Astronomy (Astropy Collaboration et al. 2013; The Astropy Collaboration et al. 2018).

DATA AVAILABILITY

The data underlying this article were accessed from the ALMA science archive¹. The derived data generated in this research will be shared on reasonable request to the corresponding author.

REFERENCES

- Alaghband-Zadeh, S., Chapman, S. C., Swinbank, A. M., et al. 2013, MNRAS, 435, 1493
- Aravena, M., Decarli, R., Walter, F., et al. 2016, ApJ, 833, 68
- Armus, L., Mazzarella, J. M., Evans, A. S., et al. 2009, PASP, 121, 559
- Astropy Collaboration, Robitaille, T. P., Tollerud, E. J., et al. 2013, A&A, 558, A33
- Barvainis, R., Maloney, P., Antonucci, R., et al. 1997, ApJ, 484, 695
- Bisbas, T. G., van Dishoeck, E. F., Papadopoulos, P. P., et al. 2017, ApJ, 839, 90
- Blake, G. A., Sutton, E. C., Masson, C. R., et al. 1987, ApJ, 315, 621
- Bolatto, A. D., Wolfire, M., & Leroy, A. K. 2013, ARA&A, 51, 207
- Bothwell, M. S., Aguirre, J. E., Aravena, M., et al. 2017, MNRAS, 466, 2825
- Carilli, C. L., & Walter, F. 2013, ARA&A, 51, 105

¹ <http://almascience.eso.org/aq/>

- Clark, P. C., Glover, S. C. O., Ragan, S. E., et al. 2019, *MNRAS*, 486, 4622
- Crocker, A. F., Pellegrini, E., Smith, J.-D. T., et al. 2019, *ApJ*, 887, 105
- Downes, D., & Solomon, P. M. 1998, *ApJ*, 507, 615
- Eales, S., Smith, M. W. L., Auld, R., et al. 2012, *ApJ*, 761, 168
- Frerking, M. A., Keene, J., Blake, G. A., et al. 1989, *ApJ*, 344, 311
- Garay, G., Mardones, D., & Mirabel, I. F. 1993, *A&A*, 277, 405
- Gerin, M., & Phillips, T. G. 2000, *ApJ*, 537, 644
- Glover, S. C. O., & Clark, P. C. 2016, *MNRAS*, 456, 3596
- Groves, B. A., Schinnerer, E., Leroy, A., et al. 2015, *ApJ*, 799, 96
- Heintz, K. E., & Watson, D. 2020, *ApJ*, 889, L7
- Herrero-Illana, R., Pérez-Torres, M. Á., Randriamanakoto, Z., et al. 2017, *MNRAS*, 471, 1634
- Hodge, J. A., & da Cunha, E. 2020, *arXiv e-prints*, arXiv:2004.00934
- Hollenbach, D. J., & Tielens, A. G. G. M. 1997, *ARA&A*, 35, 179
- Hughes, T. M., Ibar, E., Villanueva, V., et al. 2017, *MNRAS*, 468, L103
- Iono, D., Wilson, C. D., Takakuwa, S., et al. 2007, *ApJ*, 659, 283
- Israel, F. P., & Baas, F. 2001, *A&A*, 371, 433
- Israel, F. P., & Baas, F. 2003, *A&A*, 404, 495
- Israel, F. P., Rosenberg, M. J. F., & van der Werf, P. 2015, *A&A*, 578, A95
- Izumi, T., Wada, K., Fukushige, R., et al. 2018, *ApJ*, 867, 48
- Jiao, Q., Zhao, Y., Zhu, M., et al. 2017, *ApJ*, 840, L18
- Jiao, Q., Zhao, Y., Lu, N., et al. 2019, *ApJ*, 880, 133
- Kamenetzky, J., Rangwala, N., Glenn, J., et al. 2016, *ApJ*, 829, 93
- Krips, M., Martín, S., Sakamoto, K., et al. 2016, *A&A*, 592, L3
- Liu, D., Schinnerer, E., Groves, B., et al. 2019, *arXiv e-prints*, arXiv:1910.12883
- McMullin, J. P., Waters, B., Schiebel, D., et al. 2007, *Astronomical Data Analysis Software and Systems XVI*, 127
- Miyamoto, Y., Seta, M., Nakai, N., et al. 2018, *PASJ*, 70, L1
- Nesvadba, N. P. H., Cañameras, R., Kneissl, R., et al. 2019, *A&A*, 624, A23
- Offner, S. S. R., Bisbas, T. G., Bell, T. A., et al. 2014, *MNRAS*, 440, L81
- Ojha, R., Stark, A. A., Hsieh, H. H., et al. 2001, *ApJ*, 548, 253
- Oka, T., Yamamoto, S., Iwata, M., et al. 2001, *ApJ*, 558, 176
- Papadopoulos, P. P., & Greve, T. R. 2004, *ApJ*, 615, L29
- Papadopoulos, P. P., Thi, W.-F., & Viti, S. 2004, *MNRAS*, 351, 147
- Papadopoulos, P. P., Bisbas, T. G., & Zhang, Z.-Y. 2018, *MNRAS*, 478, 1716
- Phillips, T. G., & Huggins, P. J. 1981, *ApJ*, 251, 533
- Rangwala, N., Maloney, P. R., Glenn, J., et al. 2011, *ApJ*, 743, 94
- Risaliti, G., Gilli, R., Maiolino, R., et al. 2000, *A&A*, 357, 13
- Rosenberg, M. J. F., van der Werf, P. P., Aalto, S., et al. 2015, *ApJ*, 801, 72
- Saito, T., Iono, D., Yun, M. S., et al. 2015, *ApJ*, 803, 60
- Saito, T., Iono, D., Xu, C. K., et al. 2017, *ApJ*, 835, 174
- Saintonge, A., Catinella, B., Cortese, L., et al. 2016, *MNRAS*, 462, 1749
- Sakamoto, K., Aalto, S., Combes, F., et al. 2014, *ApJ*, 797, 90
- Salak, D., Nakai, N., Seta, M., et al. 2019, *arXiv e-prints*, arXiv:1911.04077
- Sandstrom, K. M., Leroy, A. K., Walter, F., et al. 2013, *ApJ*, 777, 5
- Scoville, N., Aussel, H., Sheth, K., et al. 2014, *ApJ*, 783, 84
- Scoville, N., Sheth, K., Aussel, H., et al. 2016, *ApJ*, 820, 83
- Shangguan, J., Ho, L. C., Li, R., et al. 2019, *ApJ*, 870, 104
- Shimajiri, Y., Sakai, T., Tsukagoshi, T., et al. 2013, *ApJ*, 774, L20
- Sliwa, K., Wilson, C. D., Matsushita, S., et al. 2017, *ApJ*, 840, 8
- Solomon, P. M., & Vanden Bout, P. A. 2005, *ARA&A*, 43, 677
- Tadaki, K., Iono, D., Yun, M. S., et al. 2018, *Nature*, 560, 613
- Tanaka, K., Oka, T., Matsumura, S., et al. 2011, *ApJ*, 743, L39
- Tateuchi, K., Konishi, M., Motohara, K., et al. 2015, *ApJS*, 217, 1
- The Astropy Collaboration, Price-Whelan, A. M., Sipőcz, B. M., et al. 2018, *arXiv:1801.02634*
- U, V., Sanders, D. B., Mazzarella, J. M., et al. 2012, *ApJS*, 203, 9
- Ueda, J., Iono, D., Petitpas, G., et al. 2012, *ApJ*, 745, 65
- Valentino, F., Magdis, G. E., Daddi, E., et al. 2018, *ApJ*, 869, 27
- Valentino, F., Magdis, G. E., Daddi, E., et al. 2020, *ApJ*, 890, 24
- Walter, F., Weiß, A., Downes, D., et al. 2011, *ApJ*, 730, 18
- Weiß, A., Henkel, C., Downes, D., et al. 2003, *A&A*, 409, L41
- Wilson, C. D., Scoville, N., Madden, S. C., et al. 2000, *ApJ*, 542, 120
- Wilson, C. D., Petitpas, G. R., Iono, D., et al. 2008, *ApJS*, 178, 189
- Young, J. S., & Scoville, N. Z. 1984, *ApJ*, 287, 153

This paper has been typeset from a $\text{\TeX}/\text{\LaTeX}$ file prepared by the author.